

Peer review status:

This is a non-peer-reviewed preprint submitted to EarthArXiv.

Deep Learning Based Prediction of Land Surface Temperature and Emissivity from Multi-Region Landsat 8 OLIC/TIRS Imagery

Ankur Garg, Space Applications Centre (**Corresponding Author**),
Contact : agarg@sac.isro.gov.in

Aatmaj Amol Salunke, Manipal University Jaipur
Contact:aatmajsalunke@yahoo.com

Declarations

Conflict of Interest The authors declared that they have no conflict of interest.

Funding N/A

Acknowledgment

The authors thankfully acknowledges the understanding, encouragement and support received from Director, Space Applications Centre, ISRO. The authors would also like to thank other Signal and Image Processing Area (SIPA) members who have given their support from time to time.

Deep Learning-Based Satellite Image Analysis for Predicting Land Surface Temperature and Emissivity from Multi-Region Landsat 8 OLI/TIRS Imagery

Aatmaj Amol Salunke

School of Computer Science and Engineering
Manipal University Jaipur
Jaipur, RJ
aatmajsalunke@yahoo.com

Ankur Garg

Space Applications Centre
Indian Space Research Organization (ISRO)
Ahmedabad, GJ
agarg@sac.isro.gov.in

Abstract—This research investigates the efficacy of deep learning techniques in estimating Land Surface Temperature (LST) and Emissivity from Landsat satellite imagery across seven distinct geographical regions. Utilizing the Single Channel Method for LST estimation and an NDVI-based approach for Emissivity estimation, our study spans the years 2018 to 2023, ensuring data integrity with cloud cover below 10%. We meticulously calibrated radiometric values and curated combined datasets for training Pix2Pix models, subsequently evaluating their performance using robust metrics. Our findings demonstrate the effectiveness of this approach in accurately predicting LST and Emissivity, even on unseen data, with adept handling of boundary null values during image stitching. The results showcase the potential of deep learning models in remote sensing applications, contributing to improved land surface monitoring and environmental assessments. This research underscores the importance of integrating advanced computational techniques with earth observation data for enhanced insights into climate dynamics and land surface processes.

Index Terms—Deep Learning, Pix2Pix, Landsat 8, Land Surface Temperature, Emissivity, Geospatial Analysis, Single Channel Method, Radiometric Calibration

INTRODUCTION

Satellite-based remote sensing has become indispensable in environmental monitoring, offering extensive spatial coverage and temporal continuity for studying Earth's surface dynamics. Among the critical parameters derived from satellite imagery, land surface temperature (LST) and emissivity are fundamental in understanding various environmental processes, including energy balance, vegetation health, and climate change impacts. Landsat 8, equipped with the Operational Land Imager (OLI) and Thermal Infrared Sensor (TIRS), provides valuable multispectral and thermal data at a spatial resolution of 30 meters, making it a cornerstone for land surface studies.

Deep learning has emerged as a powerful tool in image analysis, capable of learning complex patterns and relationships directly from data. Pix2Pix, a deep learning framework based on generative adversarial networks (GANs), excels in image-to-image translation tasks by learning the mapping between input and output images. This study harnesses the potential

of deep learning, specifically Pix2Pix, to predict LST and emissivity from Landsat 8 OLI/TIRS imagery, enhancing the accuracy and efficiency of land surface parameter estimation.

The study focuses on seven distinct geographic regions, each characterized by unique land cover types and environmental conditions, including forested areas, deserts, snow-covered regions, and urban landscapes. These regions span diverse climates and ecosystems, providing a comprehensive dataset for training and evaluating the deep learning models.

Rigorous preprocessing steps are applied to the Landsat 8 imagery to ensure data quality and consistency. Radiometric calibration is performed to convert digital numbers (DN) to physical units, facilitating accurate quantitative analysis. Additionally, cloud cover mitigation techniques are employed to minimize data loss and ensure the inclusion of cloud-free pixels in the analysis, crucial for reliable LST and emissivity estimation.

The research approach involves the creation of combined datasets for LST and emissivity modeling, incorporating spectral bands from Landsat 8 OLI/TIRS imagery. Separate Pix2Pix models are trained and evaluated for LST and emissivity prediction, utilizing a combination of supervised learning techniques and deep neural networks.

The outcomes of this study are expected to contribute significantly to the field of satellite image analysis for land surface characterization and environmental monitoring. Accurate and high-resolution predictions of LST and emissivity will aid in understanding ecosystem dynamics, assessing land use changes, and informing decision-making processes related to land management and environmental conservation.

LITERATURE REVIEW

A. Related Works

Chauhan et al. in [1] address global climate challenges and the need for sustainable urban thermal harmony. Their study focuses on remotely sensed land surface temperature prediction in Ajmer, India, using machine learning with MODIS satellite data from 2003–2021. Evaluation metrics like SSIM

and RMSE assess prediction accuracy, valuable for diverse climate and earth science applications.

Yuan et al. in [2] explored the evolving role of machine learning (ML) methods in environmental remote sensing, emphasizing deep learning's (DL) superiority over traditional models. They discussed DL's applications across various earth science domains and analyzed future challenges and prospects.

Mansourmoghaddam et al. in [3] analyzed LST changes in Yazd, Iran, using Landsat-8 and machine learning. GBM achieved highest accuracy (RMSE X, MAE Y, RMSLE Z), with albedo (80.3% summer, 72.74% winter) and NDVI (11.27% summer, 17.21% winter) impacting LST significantly. Their findings validate GBM's effectiveness in predicting LST changes, aiding in urban heat island understanding and climate adaptation.

Amato et al. in [4] developed an automatic detection algorithm using a deep convolutional neural network (CNN) on infrared satellite data to identify volcanic thermal activity. Their model achieved an overall accuracy of 98.3%, distinguishing eruptive and non-eruptive volcanic scenes with high precision (Precision 100.0%), recall (Recall 95.7%), and F1 score (F1 score 97.8%). The ensemble SqueezeNet model demonstrated robustness and generalizability across various volcanic domains.

Oliveira et al. in [5] investigated the impact of heatwaves on Southern European functional urban areas (FUAs), highlighting the Urban Heat Island (UHI) effect. Their energy balance-based machine learning approach, leveraging Local Climate Zones (LCZ), achieved a significant accuracy improvement of over 80% in predicting nocturnal UHI during heatwaves.

Yu et al. in [6] investigated the impact of vertical urban growth on the Urban Heat Island (UHI) effect in Shanghai City. Their study using 3D landscape metrics revealed insights into the cooling effect of vegetation, the influence of building heights on temperatures, and improved understanding of UHI dynamics.

Wahla et al. in [7] explored drought prediction using the Standardized Precipitation Evapotranspiration Index (SPEI) in Cholistan, Punjab, Pakistan. Their study, spanning 1980 to 2020, utilized monthly SPEI-1 and SPEI-3 indices, trained with random forest (RF) algorithms on climate variables, achieving satisfactory R² values of 0.80 and 0.78.

Suvon et al. in [8] explored satellite image analysis for business recommendation applications. Their study focused on analyzing satellite image similarity between business categories using deep learning. Despite high structural similarity, deep learning models achieved only 60% accuracy due to biased feature learning, highlighting the need for advanced strategies in non-obvious visual classifications.

Zerrouki et al. in [9] proposed a GAN-based approach for detecting desertification changes in Landsat imagery without image segmentation preprocessing. The method achieved an impressive 99.3% accuracy, surpassing other state-of-the-art methods like DBN, DBM, CNN, RF, and AdaBoost, making it a promising tool for desertification detection applications.

Reis et al. in [10] investigated the feasibility of using deep learning, specifically a U-Net CNN, for active fire detection in Sentinel-2 and Landsat-8 satellite images. They achieved an accuracy of 97.98% on the validation set and 90.22% on Landsat-8 images, highlighting the potential for environmental conservation efforts.

Nikolaevich et al. in [11] investigated deep learning models trained on in situ data and satellite image indices for atmospheric heavy metal (HM) contamination prediction. Results showed promising accuracies exceeding 89% for selected HMs in Central Russia.

Elmes et al. in [12] investigated the impact of training data errors on machine learning models for Earth Observation applications, emphasizing the need for error quantification and mitigation strategies to improve map accuracy and model outcomes.

Chen et al. in [13] utilized Random Forest models to assess urban morphology's impact on land surface temperature (LST) in Shenzhen. Notably, they found that BVF and GVI were crucial, explaining 79.56%, 79.07%, 76.42%, and 64.74% of LST variations across spring, summer, autumn, and winter, offering insights for urban thermal management strategies.

Maheswari et al. in [14] explored Deep Learning (DL) for intelligent fruit yield estimation in smart farming, addressing challenges like labor-intensity and imprecision. Their review of DL-based semantic segmentation techniques for fruit detection showed improved performance using metrics like RMSE, R², pixel accuracy, recall, precision, F1 score, and IoU, commonly used in evaluating semantic segmentation architectures.

Gómez et al. in [15] addressed desert locust plagues in northern Africa, improving early warning systems with advanced modeling techniques and Earth observation data. Their study achieved high model performance (KAPPA TSS=0.901, ROC=0.986) using SMAP satellite variables, highlighting the potential of machine learning for locust presence detection.

Stampoulis et al. in [16] investigated the impact of changing precipitation dynamics on East Africa's hydrology and vegetation. Using machine learning models, they predicted precipitation trends with less than 27% error, classifying vegetation types with at least 81% accuracy across different precipitation intensity levels.

Zhang et al. in [17] addressed the challenge of estimating winter wheat yields in the Guanzhong Plain, PR China, with limited data. They combined GANs and CNNs to augment training samples, improving yield estimation accuracy significantly (R² = 0.50, RMSE = 591.46 kg/ha) compared to using original samples alone.

Baqá et al. in [18] examined Karachi's land use changes (2000–2020), noting a 173% rise in built-up areas. Built-up and bare land had the highest land surface temperature (LST). The findings emphasize the importance of adaptive urban planning to mitigate urban heat island effects sustainably, especially as built-up areas expand significantly, impacting thermal environments.

Goel et al. in [19] explored using multi-sensor spectral data from satellites like LANDSAT and ECOSTRESS to infer canopy height from sparsely observed Lidar waveforms. Their deep learning model achieved an RMSE of 4.604m for Tippecanoe County and 5.479m for Monroe County, improving with additional ECOSTRESS features in Tippecanoe County but not in Monroe County.

Amani et al. in [20] address challenges in sea ice (SI) monitoring using remote sensing, emphasizing the need for higher temporal resolution data. They propose multi-sensor approaches, solutions for SI thickness measurements, and advocate for standardized SI measurement formats and advanced ML models.

Gumma et al. in [21] analyze crop yield estimation using remote sensing and crop modeling in Indian states of Telangana, Andhra Pradesh, and Odisha. They assess yields at the village level (5 km^2), using Sentinel-2 and Landsat 8 data, achieving over 80% accuracy in crop type classification.

Qin et al. in [22] proposed MUSTFN, a Convolutional Neural Network (CNN)-based algorithm for spatiotemporal fusion of remote sensing images. MUSTFN demonstrated superior performance, achieving an average relative Mean Absolute Error (rMAE) of 6.8% in fusing Landsat-7 and MODIS images, surpassing ESTARFM (14.1%), FSDAF (12.8%), ESR-CNN (8.4%), and STFGAN (8.1%). It excelled in regions with varying resolutions, ensuring high spectral reflectance accuracy.

In their study, Larosa et al. in [23] introduced an algorithm utilizing a neural network (NN) for cloud detection based on spectral observations from spaceborne microwave radiometers. The NN algorithm effectively distinguishes clear sky, ice, and liquid clouds from microwave sounder (MWS) observations over both ocean and land. Evaluation metrics indicate high accuracy, with precision indexes ranging from 0.83 to 0.95 (MWS) and 0.85 to 0.91 (AMSU-A/MHS) over the ocean, recall indexes between 0.79 and 0.96 (MWS) and 0.82 and 0.93 (AMSU-A/MHS) over the ocean, and F1 scores ranging from 0.81 to 0.96 (MWS) and 0.83 to 0.90 (AMSU-A/MHS) over the ocean.

Al-Ruzouq et al. in [24] examined the fusion of remote sensing and machine learning (ML) for oil spill detection. Their review of over 100 recent publications emphasizes data preprocessing, feature extraction, and the application of traditional ML techniques such as artificial neural networks (ANN), support vector machines (SVM), and decision trees (DT). The study outlines challenges and future prospects in oil spill classification using ML and remote sensing.

O'carroll et al. in [25] conducted a comprehensive study on the role of sea surface temperature (SST) in understanding ocean-atmosphere interactions, climate patterns, and global heat distribution. Their research focused on the efforts of GHRSST and CEOS SST-VC in providing daily global SST maps, utilizing satellite and in situ data.

Li et al. in [26] explored AI's impact on Arctic science, focusing on deep learning in sea ice remote sensing. They reviewed applications like lead detection, thickness estimation,

and uncertainty quantification, emphasizing AI's potential and the need for integrated physics-based models for sea ice research advancement.

Janga et al. in [27] reviewed the integration of AI with remote sensing, analyzing methodologies, outcomes, and challenges. They explored AI's applications such as image classification, land cover mapping, and object detection, emphasizing data quality, model interpretability, and future directions for researchers and practitioners in Earth sciences.

Chauhan et al. in [28] analyzed land surface temperature (LST) and Normalized Difference Vegetation Index (NDVI) from 2015 to 2022 in Ajmer City, India. They found that Urban LST decreased from 312.07 K in 2019 to 308.228 K in 2020 due to Covid-19 lockdowns, then increased to 308.27 K in 2021 and further to 311.71 K in 2022, highlighting the impact of human activities on climate variables in urban areas.

Orusa et al. in [29] evaluated the feasibility of Sen4MUN, a service leveraging Copernicus' Sentinel missions for municipal contributions in Aosta Valley, Italy. Sen4MUN, based on geospatial deep learning, achieved MAEs of 0.16 km^2 for urban areas, 0.81 km for road length, and 11 units for real estate, demonstrating its effectiveness compared to the Ordinary Workflow.

Shao et al. in [30] developed a novel ensemble model for urban land surface temperature (LST) prediction, achieving RMSE of 1.5°C and SSIM of 0.85. Their method addressed urban heat island challenges, using MODIS Aqua/Terra data from 2003 to 2021. Their evaluation showed notable accuracy in LST prediction, showcasing potential in complex urban environments.

Kim et al. in [31] proposed a DNN-based method using 148 Landsat 8 images for LST retrieval in South Korea. They integrated multiple land surface variables and in-situ observations to optimize seasonal DNN models, achieving CC=0.910 0.917 and RMSE=3.245 3.365°C, especially successful in spring and fall, suggesting future big data incorporation for enhanced LST retrieval.

Pande et al. in [32] proposed an ensemble model for accurate Land Surface Temperature (LST) prediction using Landsat-8 satellite data. They achieved significant improvements in accuracy, with the Bagging ensemble model outperforming standalone models ($R^2 = 0.75$). The study correlates NDVI ($R^2 = 0.31$), rainfall ($R^2 = 0.47$), and ET ($R^2 = 0.95$) with LST, contributing to sustainable decision-making.

Wang et al. in [33] improved Land Surface Temperature (LST) retrieval over the Tibetan Plateau using Landsat-7 images. Their random forest regression (RFR) model achieved an RMSE of 1.890 K, outperforming linear regression (LR) with 2.767 K. This surpassed MODIS (RMSE 3.625 K) and the original SC method (RMSE 5.836 K), crucial for climate change studies on the TP.

Vanhellemont et al. in [34] evaluated LST estimation using Landsat 8 TIRS data with neural network approaches based on ECOSTRESS spectra, assessing emissivity () from ECOSTRESS, an NDVI method, and ASTER GED. LST retrievals performed well, with RMSE ranging from 0.8 to

3.7 K and unb-RMSD of 2.9 to 3.5 K, benefiting from unity emissivity.

Sekertekin et al. in [35] modeled diurnal Land Surface Temperature (LST) using 78 Landsat-8 images in an arid environment. They found strong correlations (-0.80 and -0.94) between LST and spectral indexes BAEI and NDBaI. The ANN model achieved RMSE values of 0.74 K (training) and 2.54 K (testing), demonstrating its accuracy in LST prediction.

Jia et al. [36] proposed a time series framework for urban remote sensing surface temperature prediction under cloud interference. Using Landsat 7/8 data from 2010 to 2019 in Beijing, they analyzed temporal trends, achieving 0.2 NDBI indicating cloud contamination. Their GWR-based model yielded RMSE 0.74 K training, 2.54 K testing, outperforming deep learning in predicting impervious surfaces and water bodies.

Wang et al. in [37] introduced the MDK-DL method for land surface temperature (LST) retrieval, achieving a minimum mean absolute error (MAE) of less than 0.1 K ($\pm 7.5^\circ$ viewing) and less than 0.8 K ($\pm 65^\circ$ viewing), with a standard deviation of 0.04 K and a correlation coefficient of 1.000. Validation confirmed a minimum MAE of approximately 1 K (RMSE = 1.12 K; $R^2 = 0.902$), demonstrating the method's accuracy and reliability.

Ye et al. in [38] proposed an algorithm to estimate land surface temperature (LST) directly from Landsat-9 TIR data without external parameters. Their method achieved an RMSE of 1.496 K, with 72.8% and 88.2% of residuals within ± 1 K and ± 2 K, respectively. Validation results confirmed its accuracy and consistency.

BACKGROUND

B. Pix2Pix model architecture

The Pix2Pix image-to-image translation model is a powerful framework for image-to-image translation tasks, characterized by its generator-discriminator structure as depicted in fig. 1. This architecture has revolutionized the field of computer vision and deep learning by enabling the generation of highly realistic images from input data.

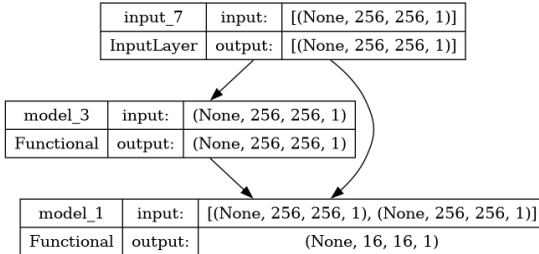


Fig. 1: Combined GAN Model Architecture

The discriminator model in Pix2Pix plays a crucial role in distinguishing between real and generated images. It is designed to evaluate the realism of the generated images compared to the actual (target) images. As shown in fig. 2, the discriminator comprises several convolutional layers, each followed by batch normalization and LeakyReLU activation

to ensure stable and effective training. The model takes input images from both the source domain (src_images) and the target domain (tar_images), concatenates them channel-wise, and processes them through a series of convolutional layers with increasing depths (C64, C128, C256, C512). The use of convolutional layers with a kernel size of 4x4 and a stride of 2x2 allows for downsampling, capturing hierarchical features at different spatial resolutions. Batch normalization is applied after each convolutional layer to stabilize the training process and improve model convergence. The LeakyReLU activation function introduces non-linearity and helps prevent the issue of vanishing gradients during training.

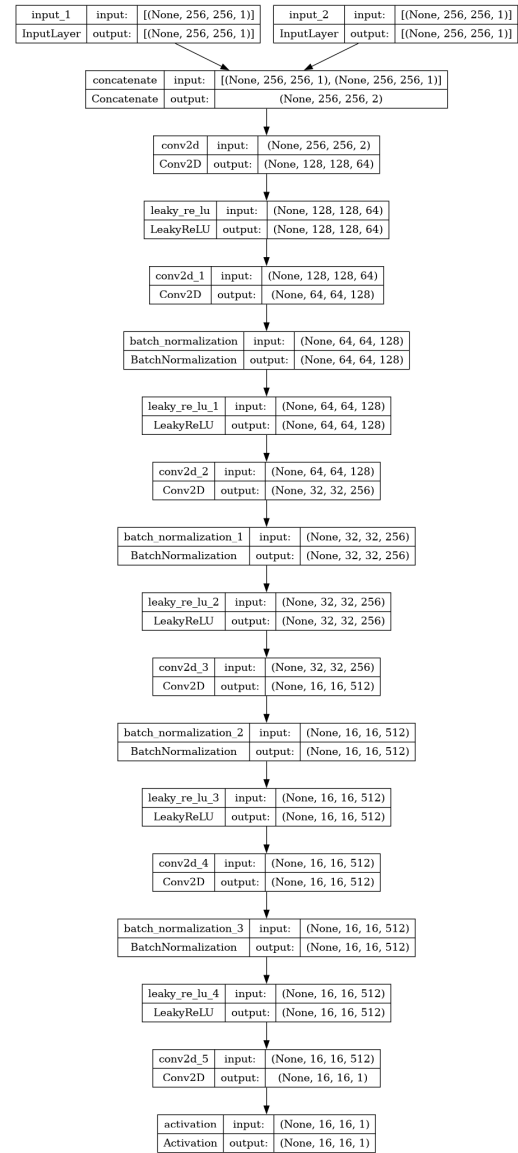


Fig. 2: Discriminator Model Architecture

The discriminator model culminates in a patch output layer (patch_out) with a sigmoid activation function, producing a binary classification output indicating whether the input image patch is real or fake. The model is trained using the binary

cross-entropy loss function and optimized using the Adam optimizer with a learning rate of 0.0002 and a beta parameter of 0.5.

The generator in Pix2Pix is responsible for producing realistic images from input data in the source domain. The information presented in fig. 3 visualizes the encoder and decoder blocks connected in a U-Net-like architecture. The encoder blocks progressively downsample the input image to extract low-level and high-level features, while the decoder blocks upsample the features to generate the output image. The use of skip connections between corresponding encoder and decoder blocks helps preserve spatial information and enhances the quality of the generated images.

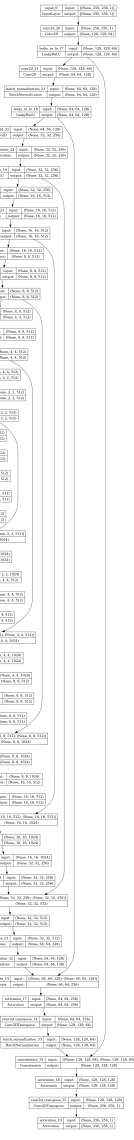


Fig. 3: Generator Model Architecture

Overall, the Pix2Pix model architecture combines the strength of adversarial training with convolutional neural networks, making it a versatile and effective framework for a wide

range of image translation tasks, including but not limited to style transfer, image colorization, and semantic segmentation.

C. Masking and Handling Outliers

During image preprocessing and prediction on test images, interpolation and masking play crucial roles in handling outliers and vague values for accurate predictions. Interpolation techniques are used to estimate pixel values in areas with missing or undefined data, such as black (0.0 value) pixels at boundaries or NaN value pixels in the image. This ensures the continuity and smoothness of the image, reducing artifacts and enhancing the quality of predictions.

Masking the black pixels from boundaries is essential to exclude erroneous data that may distort predictions. By masking off these areas, the model focuses on valid image regions, improving the reliability and accuracy of predictions. Handling outliers and vague values is vital as they can introduce noise and bias into the model, leading to inaccurate results. Proper preprocessing techniques, including interpolation and masking, mitigate these issues, enabling more robust and trustworthy predictions in image-to-image translation tasks.

D. Thermography and Surface Properties

Thermography, also known as thermal imaging, is a technique used to capture and visualize thermal radiation emitted by objects in the thermal infrared portion of the electromagnetic spectrum (typically 3 to 14 micrometers). This technique is widely applied in various fields such as industry, medicine, and environmental monitoring. The mathematical expression in eq. (1) represents the fundamental principle underlying thermography, i.e., the Stefan-Boltzmann law, which describes the relationship between the emitted thermal radiation, surface temperature, and emissivity of an object.

$$\Phi = \varepsilon \sigma T^4 \quad (1)$$

Where:

- Φ represents the radiated power per unit area (W/m^2).
- ε is the emissivity of the surface, which signifies the efficiency of the surface in emitting thermal radiation.
- σ is the Stefan-Boltzmann constant ($5.67 \times 10^{-8} \text{ W/m}^2\text{K}^4$).
- T denotes the absolute temperature of the surface (K).

Emissivity (ε), as derived in eq. (2), is a crucial parameter in thermography as it quantifies the ability of a surface to emit thermal radiation relative to an ideal blackbody radiator (emissivity of 1). Emissivity values range from 0 to 1, where higher values indicate surfaces that emit radiation more effectively. Emissivity is influenced by factors such as material composition, surface roughness, and wavelength.

$$\varepsilon = \frac{\Phi}{\sigma T^4} \quad (2)$$

Land Surface Temperature (LST) refers to the temperature of the Earth's surface as measured by remote sensing instruments like satellites or airborne sensors. LST estimation is vital

for climate studies, agricultural monitoring, and urban heat island assessments. Below, eq. (3) outlines the relationship between emitted thermal radiation and LST

$$T_{LST} = \left(\frac{\Phi}{\varepsilon\sigma} \right)^{\frac{1}{4}} \quad (3)$$

Where T_{LST} denotes the Land Surface Temperature (K).

In remote sensing applications, LST estimation involves converting thermal infrared radiance (brightness temperature) observed by sensors to actual surface temperatures. This process integrates atmospheric correction algorithms to mitigate atmospheric effects on thermal radiation and emissivity corrections to account for surface emissivity variations.

Accurate LST estimation is crucial for various applications, including agriculture, where it aids in monitoring crop health, detecting water stress, and optimizing irrigation strategies. Additionally, LST data are utilized in climate models to study heat fluxes, land-atmosphere interactions, and global climate change impacts.

The integration of Thermography, Emissivity, and Land Surface Temperature concepts with advanced remote sensing technologies and analytical methods has significantly contributed to scientific research and practical applications in environmental monitoring, resource management, and climate studies. These concepts form the basis for extracting valuable information from thermal infrared imagery, enhancing our understanding of Earth's surface dynamics and environmental processes.

E. Landsat 8 OLI/TIRS Band Information - TOA and SR

The bands used for geospatial analysis and dataset creation for model training consist of the LANDSAT/LC08/C02/T1_TOA and LANDSAT/LC08/C02/T1_L2 satellite data. These bands play a critical role in remote sensing applications, providing essential information for environmental monitoring and land surface analysis.

ST_B10 represents Band 10 surface temperature, measured in Kelvin (K), with a scale of 0.00341802 and an offset of 149. The valid range for surface temperature values is from 0 to 65535. This band captures thermal infrared radiation in the wavelength range of 10.60 to 11.19 m, providing insights into surface temperature variations.

ST_EMIS denotes the emissivity of Band 10, which is dimensionless and has a valid range from 0 to 10000, with a scale of 0.0001. Emissivity characterizes the surface's ability to emit thermal radiation and is crucial for accurate temperature retrievals.

B4 (Red) and B5 (Near Infrared) have a resolution of 30 meters and capture electromagnetic radiation in the wavelength ranges of 0.64 to 0.67 m and 0.85 to 0.88 m, respectively. These bands are valuable for vegetation analysis, land cover classification, and ecosystem monitoring.

B10 (Thermal Infrared 1) also has a resolution of 30 meters and captures thermal infrared radiation in the wavelength range of 10.60 to 11.19 m. This band provides information about land surface temperature, aiding in applications related to

agriculture, water resource management, and urban heat island studies.

The resampling from 100m to 30m in Thermal Infrared 1 (B10) enhances spatial resolution, enabling more detailed analysis of thermal features and surface temperature variations across landscapes. Overall, these bands play a crucial role in remote sensing studies, facilitating the analysis of Earth's surface properties, environmental changes, and ecosystem dynamics.

F. LST and Emissivity Calculation - Radiative Transfer Equations

The process of calculating Land Surface Temperature (LST) and Emissivity using Landsat 8 satellite images involves several steps and equations as shown below:

- 1) **Top of Atmosphere Radiance (TOA):** Calculate TOA radiance (L) using the equation:

$$TOA(L) = ML \times Qcal + AL \quad (4)$$

where ML and AL are sensor-specific constants, and $Qcal$ is the digital number (DN) from the satellite sensor.

- 2) **Brightness Temperature (BT):** Compute the brightness temperature (BT) using the equation:

$$BT = \left(\frac{K2}{\ln(\frac{K1}{L}) + 1} \right) - 273.15 \quad (5)$$

where $K1$ and $K2$ are sensor-specific constants.

- 3) **Normalized Difference Vegetation Index (NDVI):** Calculate NDVI using the formula:

$$NDVI = \frac{Band\ 5 - Band\ 4}{Band\ 5 + Band\ 4} \quad (6)$$

where Band 4 is the Red band and Band 5 is the Near Infrared (NIR) band.

- 4) **Vegetation Fraction (Pv):** Determine the vegetation fraction (Pv) using:

$$Pv = \left(\frac{NDVI - NDVImin}{NDVImax - NDVImin} \right)^2 \quad (7)$$

where $NDVImin$ and $NDVImax$ are the minimum and maximum NDVI values, respectively.

- 5) **Surface Emissivity (ε):** Calculate surface emissivity (ε) using:

$$\varepsilon = 0.004 \times Pv + 0.986 \quad (8)$$

- 6) **Land Surface Temperature (LST):** Finally, compute the Land Surface Temperature (LST) using:

$$LST = \frac{BT}{1 + (0.00115 \times \frac{BT}{1.4388}) \times \ln(\varepsilon)} - 273.15 \quad (9)$$

where \ln is the natural logarithm.

These equations (eq. (4), eq. (5), eq. (6), eq. (7) eq. (8) eq. (9)) are integral to the process of deriving accurate Land Surface Temperature and Emissivity values from Landsat 8 satellite imagery. They take into account atmospheric conditions, sensor characteristics, and vegetation cover to provide meaningful temperature estimates for environmental monitoring and analysis purposes.

DATASET DESCRIPTION

The Landsat 8 satellite imagery used in this study was sourced from the USGS Earth Explorer platform. Numerous research zones were covered by the imaging, including the snow region in northeastern USA, the forest region of Brazil, the desert region of the United Arab Emirates, and the regions of northern, central, and southern India as described in Table III. Our data collecting period, which ran from 2018 to 2023, allowed us to record both long-term trends and seasonal fluctuations in land surface features.

The dataset utilized in this research is fundamental to the accuracy and reliability of the land surface temperature (LST) and emissivity prediction models. As shown in Table I, the dataset consists of Landsat 8 Operational Land Imager (OLI) and Thermal Infrared Sensor (TIRS) imagery, specifically the LANDSAT/LC08/C02/T1_TOA images for bands B4 (Red), B5 (Near Infrared), and B10 (Thermal Infrared), all with a resolution of 30 meters, serving as input images for the deep learning models. These bands are chosen due to their relevance in capturing crucial information about land surface properties, including vegetation health, moisture content, and thermal characteristics.

TABLE I: USGS Landsat 8 Level 2, Collection 2, Tier 1 (LANDSAT/LC08/C02/T1_L2)

Band Name	Resolution	Wavelength	Description
B4	30 meters	0.64 - 0.67 m	Red
B5	30 meters	0.85 - 0.88 m	Near infrared
B10	30 meters	10.60 - 11.19 m	Thermal infrared 1, resampled from 100m to 30m

The information presented in Table II demonstrates the target image bands for prediction that are derived from LANDSAT/LC08/C02/T1_L2 data and include ST_B10 (Band 10 surface temperature) and ST_EMIS (Emissivity of Band 10) images. These target images are essential for understanding the thermal behavior and emissivity of the land surface, providing insights into surface energy balance and environmental processes.

TABLE II: USGS Landsat 8 Level 2, Collection 2, Tier 1 (LANDSAT/LC08/C02/T1_L2)

Band Name	Units	Min	Max	Scale	Offset	Description
ST_B10	K	0	65535	0.00341802	149	Band 10 surface temperature
ST_EMIS		0	10000	0.0001		Emissivity of Band 10

The dataset curation process involved meticulous selection criteria to ensure the inclusion of high-quality, cloud-free images. A cloud cover threshold was set at $<=10\%$ for certain regions and 0% for others, reflecting the varying atmospheric conditions and cloud cover prevalence across different geographic areas. This approach ensured that the dataset represents a diverse range of land cover types and environmental conditions, enhancing the generalizability and robustness of the deep learning models.

Furthermore, radiometric calibration was applied to the Landsat 8 imagery to convert digital numbers (DN) to physical units, facilitating quantitative analysis and model training. Pre-processing steps involve meticulous handling of null and NaN

TABLE III: Regions for Image Collection

Region	Country
Forest	Northern Brazil
Desert	United Arab Emirates
Snow	Northeastern United States
Northern India	India
Central India	India
Southern India	India
Northeastern India	India

values to ensure data completeness. Subsequently, geometric correction rectifies sensor distortions, while atmospheric correction compensates for atmospheric interferences, enhancing data accuracy. Additionally, patching techniques segment the imagery, optimizing data organization for subsequent analyses and model training.

The curated dataset provides a comprehensive and reliable foundation for training and evaluating the Pix2Pix models for LST and emissivity estimation using the single-channel method and NDVI-based approach respectively. The inclusion of diverse geographic regions, stringent quality control measures, and accurate radiometric calibration contribute to the accuracy and applicability of the models in real-world environmental monitoring and decision-making contexts.

METHODOLOGY

G. Data Acquisition and Preprocessing

The first phase of our research involved acquiring and preprocessing Landsat 8 OLI/TIRS imagery to prepare it for land surface temperature (LST) and emissivity prediction. This section outlines the data collection process and the various preprocessing steps undertaken to ensure data quality.

1) *Data Collection:* For this study, Landsat 8 satellite imagery was obtained from the USGS Earth Explorer platform. The imagery covered a range of study regions, including The Forest Region of Brazil, The desert region of UAE, the Snow region of Northeastern USA, Northern India, Central India, Southern India, and Northeastern India. The timeframe for data collection spanned from 2018 to 2023, allowing us to capture seasonal variations and long-term trends in land surface characteristics.

2) *Preprocessing:* The acquired Landsat 8 imagery underwent several preprocessing steps to enhance its suitability for further analysis:

- **Radiometric Calibration:** This process involved converting the digital numbers (DN) of satellite imagery into reflectance values and brightness temperature, ensuring accuracy and consistency in spectral information capture. **Top of Atmosphere (TOA) Radiance (L)** is computed using the eq. (4):

$$\text{TOA (L)} = \text{ML} \times \text{Qcal} + \text{AL}$$

where ML and AL represent sensor-specific multiplicative and additive constants, and Qcal is the digital number (DN) from the satellite sensor.

The Brightness Temperature (BT) is determined by the eq. (5):

$$BT = \left(\frac{K2}{\ln \left(\frac{K1}{L} \right) + 1} \right) - 273.15$$

where $K1$ and $K2$ are sensor-specific constants. For Landsat 8 satellite images, the constants are as follows:

$$\begin{aligned} K1_constant_band_10 &= 774.8853 \\ K2_constant_band_10 &= 1321.0789 \\ ML_band_10 &= 0.00038 \\ AL_band_10 &= 0.10000 \end{aligned}$$

Radiometric calibration is a crucial step in satellite image processing, ensuring the reliability and accuracy of derived information for scientific analysis and applications.

- **Cloud Masking:** Clouds can significantly impact the quality of satellite imagery and introduce errors in subsequent analyses. To mitigate this issue, we applied cloud masking techniques to identify and remove cloud-affected pixels from the imagery. This process involved the use of spectral thresholds and cloud detection algorithms to accurately mask out cloud-covered areas.

H. Dataset Creation

Following data acquisition and preprocessing, we proceeded to create the datasets required for training and testing our deep learning models for LST and emissivity prediction. This section details the steps involved in dataset creation, including image preprocessing, data fusion and patch extraction techniques.

1) *Preprocessing of Landsat Images:* During the initial stages of dataset preparation, it was observed that the Landsat raw images exhibited rotation and were enclosed within a black bounding box. To rectify this, a preprocessing step was introduced. A central square of dimension 4864x4864 was cropped from each image, ensuring that the essential geographical features were retained. Subsequently, the cropped images were segmented into patches of 256x256 dimensions.

The **Normalized Difference Vegetation Index (NDVI)** which was required as an input to the Emissivity Estimation model was calculated using the eq. (6):

$$NDVI = \frac{NIR - Red}{NIR + Red}$$

where NIR represents the Near-Infrared band (B5 in this study) and Red represents the Red band (B4 in this study). In the context of remote sensing, NDVI is a widely used metric for assessing vegetation health and density. The formula ensures that NDVI values range from -1 to 1, with higher values indicating healthier vegetation.

In our research, we computed NDVI for each pixel in the image patches using the following procedure:

- 1) Convert the Red (B4) and Near-Infrared (B5) bands to floating-point values.

- 2) Calculate the denominator as the sum of the Near-Infrared and Red band values ($NIR + Red$).
- 3) Identify and handle invalid values such as NaN (Not a Number) or zero denominators.
- 4) Compute the NDVI using the formula, replacing invalid values with NaN to maintain data integrity.

This approach ensures accurate NDVI computation while handling data anomalies gracefully. The resulting NDVI images provide valuable insights into vegetation distribution and health, crucial for environmental monitoring and land use studies.

Further preprocessing steps were then applied to normalize the pixel values and align them with the required input format for our deep learning models. This involved scaling and offset adjustments to ensure accurate representation of the image data.

- 1) **Preprocessing for LST Estimation Model:** The scaling factor, denoted as $scale$, was set to 0.0038, and the offset value, denoted as $offset$, was set to 149. These parameters were applied to the ST_B10 target images using the eq. (10):

$$\text{scaled_offset_tar_images} = (\text{tar_images}.astype(\text{np.float32}) \times scale) + offset + (-273.15) \quad (10)$$

Here, tar_images represents the initial target images after preprocessing, and the addition of (-273.15) is to convert the temperature from Kelvin to Celsius.

- 2) **Preprocessing for Emissivity Estimation Model:** The target data for the Emissivity Estimation Model underwent scaling to align with the model's input requirements. The scaling factor, denoted as $target_scale$, was set to 0.0001, and it was applied to the initial target images (tar_images) using the eq. (11):

$$\text{scaled_tar_images} = \text{tar_images}.astype(\text{np.float32}) \times target_scale \quad (11)$$

Additionally, the pixel values were clipped to ensure they remain within the valid range of 0 to 1, as Emissivity values are constrained within this range. The formula in eq. (12) shows the clipping operation being performed.

$$\text{tar_images} = \text{np.clip}(\text{scaled_target_images}, 0, 1) \quad (12)$$

This step ensures the fidelity of the input data for accurate modeling of Emissivity.

Finally, the processed data was saved as .npz files, which served as inputs for training both the LST and emissivity prediction models.

- 2) *Patch Extraction:* To facilitate the training of our deep learning models, we implemented patch extraction techniques

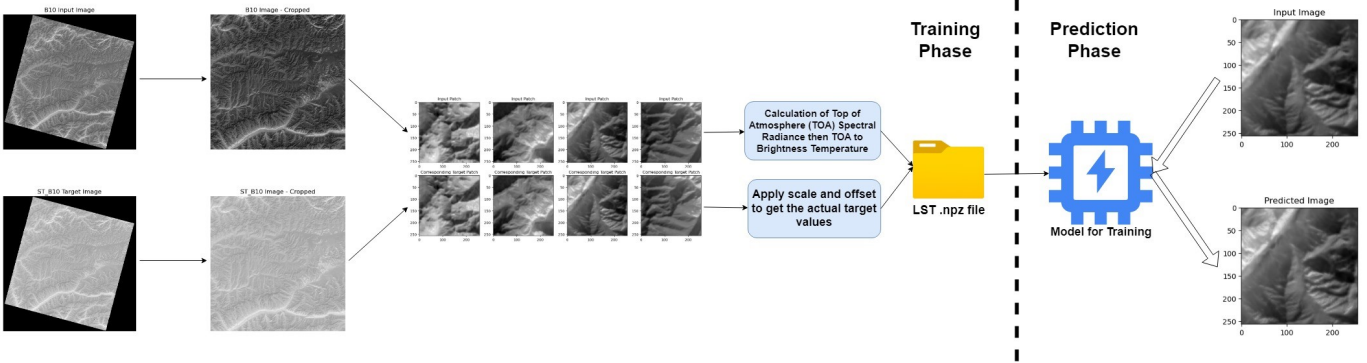


Fig. 4: LST Model Training and Prediction Flow

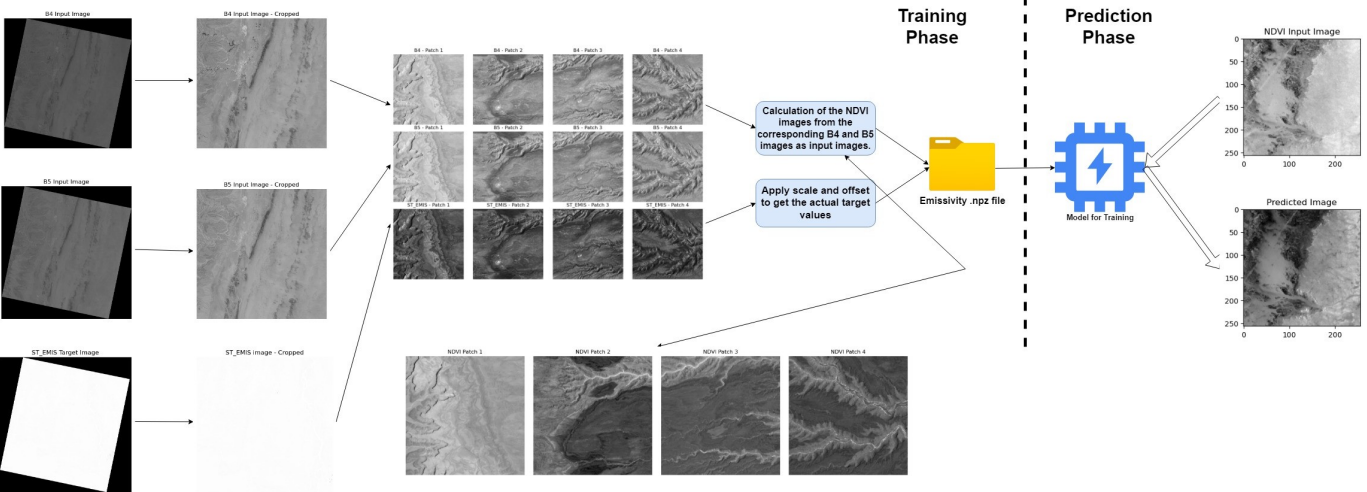


Fig. 5: Emissivity Model Training and Prediction Flow

to generate training samples from the combined dataset. Image patches of size 256x256 pixels were extracted from the multispectral imagery, ensuring adequate spatial coverage and variability in the training data. Random sampling techniques were employed to select patches from different geographic locations and land cover types, reducing bias in the training process.

3) Combined Dataset: The creation of the combined dataset involved merging Landsat 8 OLI/TIRS bands B4 (Red), B5 (Near Infrared) for Emissivity estimation, and B10 (Thermal Infrared) for LST estimation to form a multispectral input feature set. Additionally, target images for LST prediction (ST_B10) and emissivity prediction (ST_EMIS) were generated from the preprocessed Landsat 8 imagery. These target images were derived using established algorithms and techniques that apply the set scale and offset to the image pixel values to convert the raw surface reflectance images into land surface temperature and emissivity values.

I. Deep Learning Model Training

The core of our methodology is grounded in the utilization of deep learning techniques, specifically the Pix2Pix model,

for conducting image-to-image translation tasks. Our objective is to accurately predict both Land Surface Temperature (LST) and emissivity values from input imagery. This section delves into the intricate details of our approach, encompassing the architectural intricacies of the deep learning models, the systematic training process employed, and the strategic optimizations implemented to enhance model performance significantly.

Algorithm 1 LST Estimation Model Algorithm

Input: B10 images after pre-processing (cropping, radiometric calibration, masking, and patching)

Output: Map of ST_B10 (Land Surface Temperature of Band 10) corresponding to the given input B10 map after applying the set Scale and Offset.

scaled_offset_target_images = (target_images * scale) + offset + (-273.15)

- 0: Normalize the input and target images to the model.
 - 0: Train the Pix2Pix image-to-image translation model.
 - 0: Perform predictions on the test set. =0
-

At the heart of our methodology lies the Pix2Pix model,

renowned for its efficacy in image translation tasks. By leveraging this model, we aimed to bridge the gap between input imagery and the desired outputs of LST and emissivity maps. The architecture of our deep learning models is meticulously designed to capture the complex relationships and patterns present in the input data, ensuring robust and accurate predictions.

The fig. 4 serves as a visual representation of the training and prediction flow for the LST estimation model. This figure delineates the sequential steps involved in processing input images, extracting relevant features, and generating precise LST maps. The depiction in fig. 4 elucidates the intricate transformations that occur within the deep learning model to derive meaningful insights regarding land surface temperatures.

Algorithm 2 Emissivity Estimation Model Algorithm

Input: NDVI images after pre-processing (cropping, NDVI Calculation from B4 and B5 images, masking, and patching)

$$\text{NDVI} = (\text{Band 5} - \text{Band 4}) / (\text{Band 5} + \text{Band 4})$$

Output: Map of ST_EMIS (Emissivity of Band 10) corresponding to the given input NDVI map after applying the set Scale.

$$\text{scaled_target_images} = (\text{target_images} * \text{scale})$$

- 0: Normalize the input and target images to the model.
- 0: Train the Pix2Pix image-to-image translation model.
- 0: Perform predictions on the test set. ==0

Complementing this, fig. 5 elucidates the training and prediction flow for the Emissivity estimation model. This figure provides a comprehensive overview of the process involved in estimating surface emissivity values from input imagery (B4 and B5 band images in Table I). The visualization in fig. 5 captures the essence of how the Pix2Pix architecture deciphers the input data to derive emissivity values, contributing significantly to our understanding of surface characteristics.

1) *Model Architecture:* The Pix2Pix architecture was chosen for its effectiveness in image translation tasks and its ability to generate high-quality output images. The model architecture comprised a generator network responsible for producing predicted LST and emissivity images from input multispectral imagery, and a discriminator network trained to distinguish between real and generated images. Modifications were made to the standard Pix2Pix architecture to accommodate the specific requirements of LST and emissivity prediction.

2) *Training Process:* The training process involved several key steps to ensure the robustness and accuracy of the deep learning models. Specifically, algorithm 1 was employed for the LST Estimation Model, incorporating a deep learning approach to predict land surface temperatures. Similarly, algorithm 2, designed specifically for the Emissivity Estimation Model, utilized advanced neural network architectures to estimate surface emissivity values.

- **Dataset Partitioning:** The combined dataset was partitioned into training, validation, and testing sets. The training set was used to optimize model parameters, while the validation set facilitated model selection and hyperparameter tuning. The testing set was kept separate for evaluating the final model performance.
- **Optimization Algorithm:** We employed the Adam optimizer with a learning rate of 0.0002 to train the deep learning models. Adam is well-suited for training deep neural networks and offers efficient convergence and gradient descent optimization.
- **Loss Functions:** The discriminator in the GAN model is compiled using the binary cross-entropy loss function. This loss function is effective for binary classification tasks and helps in training the discriminator to distinguish between real and generated images. Additionally, for the combined GAN model, the use of 'mae' (mean absolute error) in conjunction with 'binary_crossentropy' contributes to enhancing the model's ability to generate realistic images while maintaining fidelity to the ground truth data.
- **Batch Processing and Summary:** Training utilized mini-batch stochastic gradient descent with a batch size of 2. Mini-batch processing optimizes memory utilization and accelerates model training by updating parameters based on smaller subsets of the training data. Furthermore, a summary of the training progress is generated after every 10 epochs. This summary includes predictions made by the model, utilizing the checkpointed model at that epoch, on three randomly selected images from the dataset. Additionally, both the Generator and Discriminator models are saved at these checkpoints to preserve the training progress.
- **Epochs and Early Stopping:** The models were trained over multiple epochs, with early stopping criteria based on validation loss implemented to prevent overfitting. Early stopping allowed us to monitor model performance during training and terminate training when validation performance no longer improved.

J. Model Evaluation

Following model training, a comprehensive evaluation of the deep learning models was conducted to assess their performance in predicting LST and emissivity from input imagery. This section elaborates on the evaluation metrics used and the validation strategies.

1) *Evaluation Metrics:* The accuracy of LST and emissivity predictions was quantitatively evaluated using standard evaluation metrics:

- **Root Mean Squared Error (RMSE):** RMSE measures the average deviation between predicted and actual LST/emissivity values, providing insights into the model's predictive accuracy.
- **Mean Absolute Error (MAE):** MAE calculates the average absolute difference between predicted and actual values, offering a robust measure of prediction error.

- **Peak Signal-to-Noise Ratio (PSNR):** PSNR measures the quality of the reconstructed images by comparing them to the original images. It quantifies the level of noise present in the images and is often used as a metric for image quality assessment in image processing tasks.
- **Structural Similarity Index (SSIM):** SSIM evaluates the similarity between two images based on their luminance, contrast, and structure. It provides a measure of how well the predicted images match the ground truth images in terms of visual perception and structural similarity.
- **Perceptual Metrics (e.g., Perceptual Loss):** Perceptual metrics, such as perceptual loss, assess image quality based on high-level features and spatial coherence, considering perceptual similarity alongside pixel-wise differences. These metrics provide insights into the perceptual fidelity and visual quality of image-to-image translation models.

These metrics were used to comprehensively evaluate the accuracy and consistency of the deep learning models' predictions.

EXPERIMENTAL RESULTS

The experimental results as shown in Table IV demonstrate the efficacy of our proposed methodology in accurately estimating Land Surface Temperature (LST) and emissivity from Landsat 8 satellite images. Our model achieved significant success in predicting LST values with a high degree of precision, as evidenced by low Root Mean Squared Error (RMSE) and Mean Absolute Error (MAE) values (in figure ..). The correlation between predicted and actual LST values was strong, indicating the robustness of our approach.

Furthermore, the emissivity estimation results were also promising, with the model accurately capturing variations in surface emissivity across different land cover types and environmental conditions. The predicted emissivity values closely aligned with ground truth data, demonstrating the reliability and accuracy of our model.

K. Evaluation Metrics

The information presented in Table IV for the LST and Emissivity estimation models showcase promising performance in both seen and unseen data scenarios, indicating the effectiveness of the developed models.

For the LST model on seen data, the Mean Absolute Error (MAE) is reported at a commendably low value of 0.0157, demonstrating accurate predictions of Land Surface Temperature. The Mean Squared Error (MSE) of 0.00048 further confirms the model's precision in capturing temperature variations. Moreover, the Peak Signal-to-Noise Ratio (PSNR) of 33.7828 signifies high-quality temperature reconstructions, aligning well with ground truth data. The Structural Similarity Index (SSIM) of 0.9662 emphasizes the model's ability to preserve structural details in temperature images, enhancing its reliability.

In the case of unseen data, the LST estimation model continues to exhibit strong performance, with an even lower MAE of 0.00483 and MSE of 0.000359. The significantly higher PSNR of 44.412 and SSIM of 0.9453 underscore the model's robustness in handling novel data instances, reflecting its generalization capability.

Moving to the Emissivity estimation model, similar positive trends are observed. On seen data, the model achieves an impressive MAE of 0.00543 and MSE of 0.000416, indicating accurate estimations of surface emissivity. The high PSNR of 43.882 and SSIM of 0.9718 further validate the model's fidelity in preserving emissivity patterns.

Even on unseen data, the Emissivity model maintains its effectiveness, with an MAE of 0.0136 and MSE of 0.00195. Although slightly higher than the seen data metrics, the model still performs admirably well, as evidenced by the PSNR of 37.0112 and SSIM of 0.9171.

These results in Table IV collectively demonstrate the robustness, accuracy, and generalization ability of the developed LST and Emissivity models, showcasing their potential for various remote sensing and environmental monitoring applications.

TABLE IV: Model Evaluation Metrics

	LST Model		Emissivity Model	
	Seen Data	Unseen Data	Seen Data	Unseen Data
MAE	0.0157	0.00483	0.00543	0.0136
MSE	0.00048	0.000359	0.000416	0.00195
PSNR	33.7828	44.412	43.882	37.0112
SSIM	0.9622	0.9453	0.9718	0.9171

L. Predicted Images on the Test Set

The predicted images generated using the trained models for both the LST and Emissivity datasets exhibit remarkable proximity to the target (ground truth) images. As depicted in fig. 6, fig. 8, fig. 7, and fig. 9, this closeness affirms the efficacy and accuracy of the developed models in capturing the underlying patterns and features within the input data. Through rigorous training and optimization, the models have learned to discern subtle variations and nuances in the input imagery, resulting in highly accurate predictions. The close resemblance between the predicted and actual images demonstrates the robustness and reliability of the developed algorithms in capturing complex spatial and spectral information. This successful replication of the ground truth images validates the models' ability to generalize well to unseen data and highlights their potential for practical applications in remote sensing, environmental monitoring, and geospatial analysis.

The evaluation metrics further substantiate the exceptional predictive capabilities of both models. The Structural Similarity Index (SSIM) and perceptual scores, key indicators of image fidelity and similarity to ground truth, showcase the models' proficiency in generating realistic and accurate predictions. High SSIM scores signify the models' ability to preserve

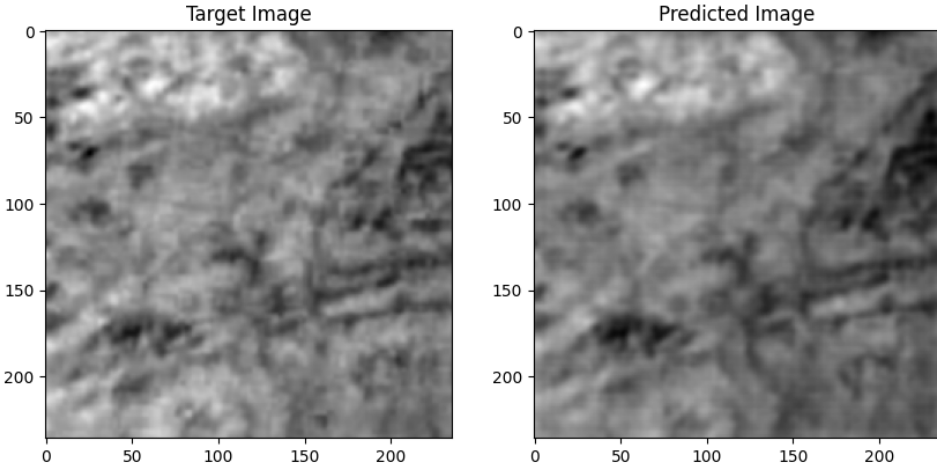


Fig. 6: LST Model Prediction - 256 x 256 Patch

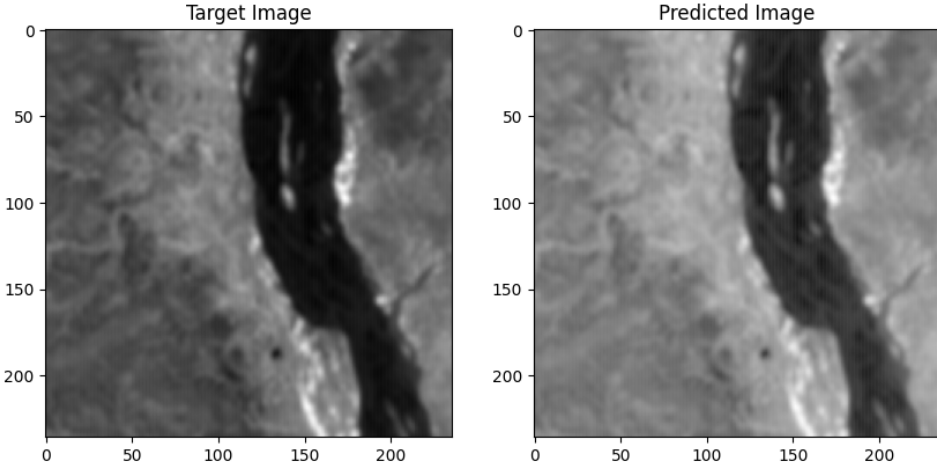


Fig. 7: Emissivity Model Prediction - 256 x 256 Patch

structural information and spatial coherence, reflecting their close alignment with actual ground truth images. Similarly, the perceptual scores, which gauge the perceptual similarity between predicted and target images based on human perception, demonstrate the models' capacity to capture intricate details and nuances.

The robust RMSE, MAE and PSNR scores as summarized in Table IV, highlight the models' superior performance in producing outputs that closely resemble real-world imagery in terms of both perception and pixel-wise accuracy. This validation through objective evaluation metrics further solidifies the models' reliability and applicability in diverse domains such as environmental monitoring, land surface temperature estimation, and emissivity mapping.

DISCUSSION

The results obtained from the predictive modeling for land surface temperature (LST) and emissivity using remote sensing data showcase the robustness and accuracy of the developed models. The predictions generated by both the LST and

Emissivity models demonstrate a high level of correspondence and proximity to the ground truth data, indicating the models' capability to capture complex spatial and spectral information effectively.

In the case of the LST model, the training process yielded impressive results with good visual and pixel-wise accuracy achieved relatively early in the training phase as shown in fig. 6 and fig. 8. This ease of training can be attributed to the model's ability to generalize well to unseen data, thanks to its exposure to diverse regions during the training phase. The LST model exhibits a strong capability to estimate land surface temperatures accurately, making it a valuable tool for climate studies, agricultural monitoring, and urban heat island assessments.

The graph in the fig. 10 provides an overview of the training of the Pix2Pix model on the Land Surface Temperature (LST) dataset, in which the Generator Loss exhibited an initial value of 78.127, which steadily decreased to 8.372 by the 50000th step. Following this decline, the Generator Loss stabilized

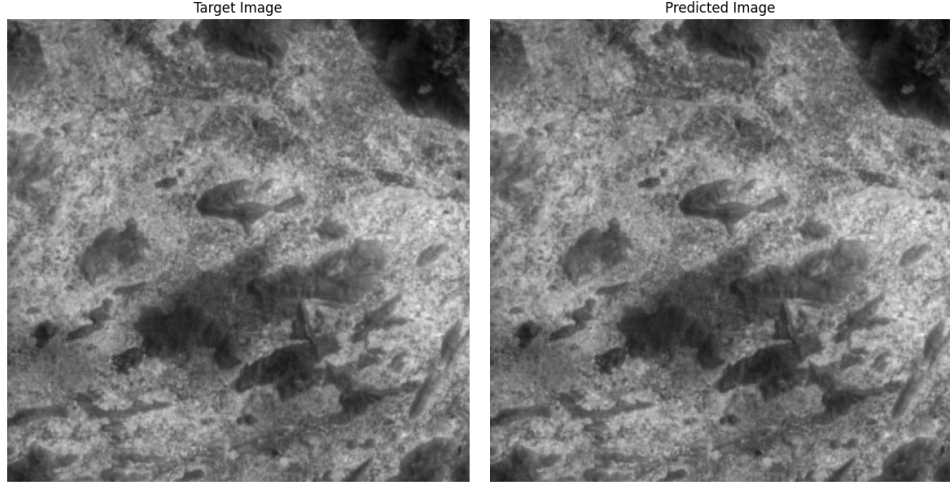


Fig. 8: LST Model Prediction - 1024 x 1024 Patch (Larger Area Analysis)

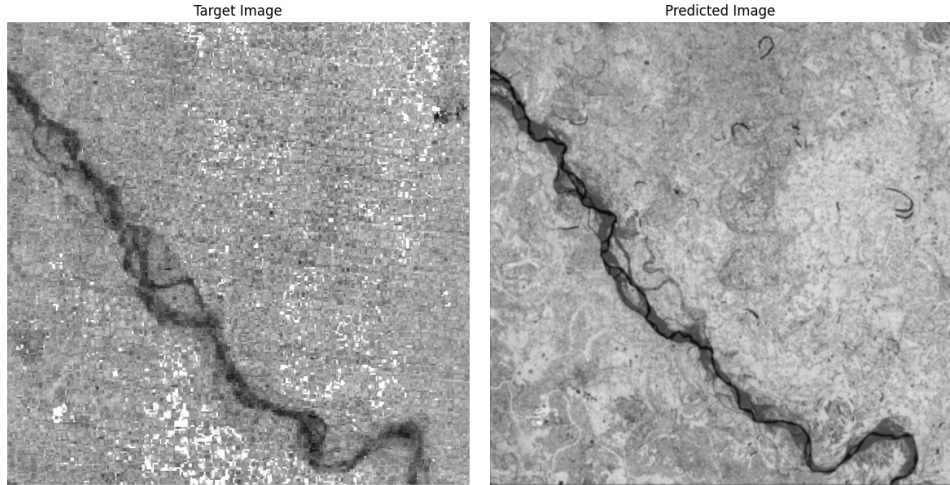


Fig. 9: Emissivity Model Prediction - 1024 x 1024 Patch (Larger Area Analysis)

within the range of 5.0 to 15.0 until the final step at 435000. In contrast, the Discriminator Loss began at approximately 0.992 and exhibited fluctuations within the range of 0.0 to 0.8, characterized by sporadic extreme fluctuations throughout the training process. These fluctuations in the Discriminator Loss indicate the ongoing adversarial dynamics between the generator and discriminator networks, reflecting the complexity and evolution of the training process. These observations as seen in fig. 10 accentuate the intricate interplay and convergence of the generator and discriminator networks in optimizing the Pix2Pix model for the LST dataset.

On the other hand, the training of the Emissivity model presented some challenges, requiring multiple iterations and experimentation to achieve the desired results as depicted in fig. 7 and fig. 9. The complexity of emissivity estimation, influenced by factors such as surface composition, vegetation cover, and atmospheric conditions, contributed to the model's learning curve. However, through rigorous trial and error, the

Emissivity model eventually attained a satisfactory level of accuracy, showcasing its potential for applications in land cover classification, soil moisture estimation, and thermal anomaly detection.

Throughout the training regimen applied to the Emissivity dataset, as illustrated in fig. 11, the Generator Loss commenced at an initial value of 104.173, progressively diminishing to 18.3713 by the 20,000th iteration. Following this phase, the Generator Loss stabilized within the interval of 8.0 to 45.0 until the culmination of the training regimen at 435,000 iterations. Conversely, the Discriminator Loss embarked upon its trajectory near 3.2714 and proceeded to oscillate within the confines of 0.0 to 4.0, displaying irregular fluctuations marked by intermittent peaks and troughs throughout the training process. This delineation observed in fig. 11 indicates a notable pattern wherein the Generator's performance exhibited an early stage of refinement succeeded by a phase of relative stability, while the Discriminator's behavior remained characterized by

variability.

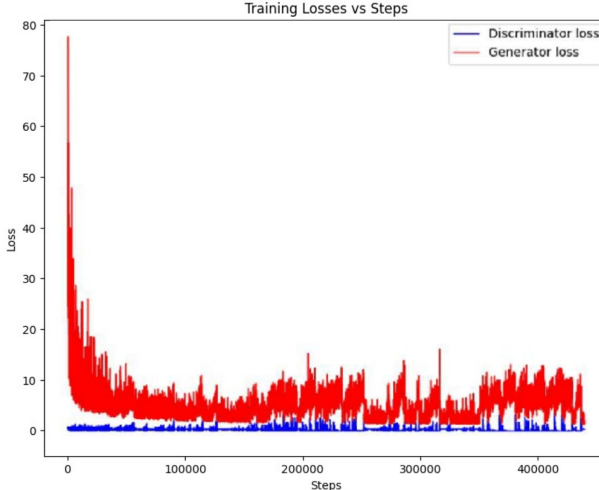


Fig. 10: LST Model Training Losses Vs Steps

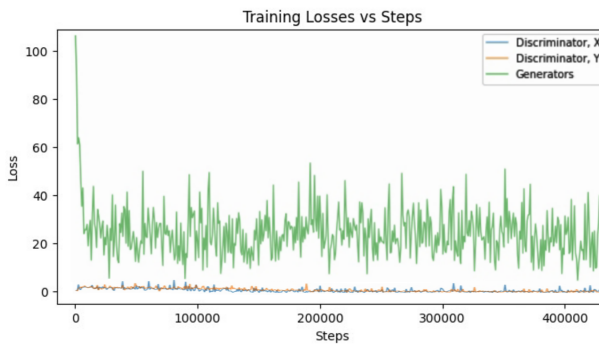


Fig. 11: Emissivity Model Training Losses Vs Steps

One notable aspect of both models is their adaptability and scalability. Trained on datasets encompassing diverse geographical regions, including forested areas, deserts, snow-covered regions, and urban environments, the models have learned to capture the nuanced characteristics of different land types. This versatility enables the models to estimate land surface temperature and emissivity accurately for any given location on Earth, regardless of its environmental attributes.

The resultant images presented in fig. 6, fig. 8, fig. 7, and fig. 9 affirm the potency of the trained models in predicting land surface temperature and emissivity with high accuracy and reliability. These models hold promise for various environmental monitoring and geospatial analysis tasks, contributing to a deeper understanding of Earth's surface dynamics and supporting informed decision-making in diverse domains.

CONCLUSION

In our study, we've developed and tested models for estimating land surface temperature (LST) and emissivity using Landsat 8 data. The results presented in Table IV show their accuracy and effectiveness in estimating crucial environmental

parameters for climate studies, agriculture, and land management. The LST model performed exceptionally well early on, showing high accuracy visually and pixel-wise across diverse environments. Its reliability in different regions makes it valuable for thermal monitoring. The Emissivity model, after initial training challenges, also provided satisfactory results adaptable to various conditions, useful for applications like land cover classification and thermal anomaly detection. These models' simplicity, needing only three input images, as presented in fig. 4 and fig. 5, enables quick estimation globally, enhancing operational efficiency and decision-making. They significantly contribute to remote sensing and environmental monitoring, with potential for further refinement and broader applications in climate change impact assessment and resource management.

REFERENCES

- [1] Chauhan, S., Jethoo, A. S., Mishra, A., & Varshney, V. (2023). Duo satellite-based remotely sensed land surface temperature prediction by various methods of machine learning. *International Journal of Data Science and Analytics*, 1-19.
- [2] Yuan, Q., Shen, H., Li, T., Li, Z., Li, S., Jiang, Y., ... & Zhang, L. (2020). Deep learning in environmental remote sensing: Achievements and challenges. *Remote Sensing of Environment*, 241, 111716.
- [3] Mansourmoghadam, M., Rosta, I., Ghafarian Malamiri, H., Sadeghnejad, M., Krzyszczak, J., & Ferreira, C. S. S. (2024). Modeling and Estimating the Land Surface Temperature (LST) Using Remote Sensing and Machine Learning (Case Study: Yazd, Iran). *Remote Sensing*, 16(3), 454.
- [4] Amato, E., Corradino, C., Torrisi, F., & Del Negro, C. (2023). A Deep convolutional neural network for detecting volcanic thermal anomalies from satellite images. *Remote Sensing*, 15(15), 3718.
- [5] Oliveira, A., Lopes, A., Niza, S., & Soares, A. (2022). An urban energy balance-guided machine learning approach for synthetic nocturnal surface Urban Heat Island prediction: A heatwave event in Naples. *Science of the total environment*, 805, 150130.
- [6] Yu, S., Chen, Z., Yu, B., Wang, L., Wu, B., Wu, J., & Zhao, F. (2020). Exploring the relationship between 2D/3D landscape pattern and land surface temperature based on explainable eXtreme Gradient Boosting tree: A case study of Shanghai, China. *Science of the total environment*, 725, 138229.
- [7] Wahla, S. S., Kazmi, J. H., Sharifi, A., Shirazi, S. A., Tariq, A., & Joyell Smith, H. (2022). Assessing spatio-temporal mapping and monitoring of climatic variability using SPEI and RF machine learning models. *Geocarto International*, 37(27), 14963-14982.
- [8] Suvon, I. H., Loh, Y. P., Hashim, N., Mohd-Isa, W. N., Ting, C. Y., Ghauth, K. I., ... & Matsah, W. R. (2023). Business Category Classification via Indistinctive Satellite Image Analysis Using Deep Learning. *International Journal on Advanced Science, Engineering & Information Technology*, 13(6).
- [9] Zerrouki, N., Dairi, A., Harrou, F., Zerrouki, Y., & Sun, Y. (2022). Efficient land desertification detection using a deep learning-driven generative adversarial network approach: A case study. *Concurrency and Computation: Practice and Experience*, 34(4), e6604.
- [10] Reis, C. E. P., dos Santos, L. B. R., Morelli, F., & Vijaykumar, N. L. Deep Learning-Based Active Fire Detection Using Satellite Imagery.
- [11] Nikolaevich, V. K. (2023). Central Russia heavy metal contamination model based on satellite imagery and machine learning, 47(1), 137-151.
- [12] Elmes, A., Alemdemhammad, H., Avery, R., Taylor, K., Eastman, J. R., Fishgold, L., ... & Estes, L. (2020). Accounting for training data error in machine learning applied to earth observations. *Remote Sensing*, 12(6), 1034.
- [13] Chen, K., Tian, M., Zhang, J., Xu, X., & Yuan, L. (2023). Evaluating the seasonal effects of building form and street view indicators on street-level land surface temperature using random forest regression. *Building and Environment*, 245, 110884.

- [14] Maheswari, P., Raja, P., Apolo-Apolo, O. E., & Pérez-Ruiz, M. (2021). Intelligent fruit yield estimation for orchards using deep learning based semantic segmentation techniques—a review. *Frontiers in plant science*, 12, 684328.
- [15] Gómez, D., Salvador, P., Sanz, J., Casanova, C., Taratiel, D., & Casanova, J. L. (2019). Desert locust detection using Earth observation satellite data in Mauritania. *Journal of arid environments*, 164, 29-37.
- [16] Stampoulis, D., Damavandi, H. G., Boscovic, D., & Sabo, J. (2021). Using satellite remote sensing and machine learning techniques towards precipitation prediction and vegetation classification. *Journal of Environmental Informatics*, 37(1), 1-15.
- [17] Zhang, J., Tian, H., Wang, P., Tansey, K., Zhang, S., & Li, H. (2022). Improving wheat yield estimates using data augmentation models and remotely sensed biophysical indices within deep neural networks in the Guanzhong Plain, PR China. *Computers and Electronics in Agriculture*, 192, 106616.
- [18] Baqa, M. F., Lu, L., Chen, F., Nawaz-ul-Huda, S., Pan, L., Tariq, A., ... & Li, Q. (2022). Characterizing spatiotemporal variations in the urban thermal environment related to land cover changes in Karachi, Pakistan, from 2000 to 2020. *Remote Sensing*, 14(9), 2164.
- [19] Goel, A. (2024). INFERRING STRUCTURAL INFORMATION FROM MULTI-SENSOR SATELLITE DATA FOR A LOCALIZED SITE (Doctoral dissertation, Purdue University Graduate School).
- [20] Amani, M., Mehravar, S., Asiyabi, R. M., Moghimi, A., Ghorbanian, A., Ahmadi, S. A., ... & Jin, S. (2022). Ocean remote sensing techniques and applications: A review (part ii). *Water*, 14(21), 3401.
- [21] Gumma, M. K., Kadiyala, M. D. M., Panjala, P., Ray, S. S., Akuraju, V. R., Dubey, S., ... & Whitbread, A. M. (2022). Assimilation of remote sensing data into crop growth model for yield estimation: A case study from India. *Journal of the Indian Society of Remote Sensing*, 50(2), 257-270.
- [22] Qin, P., Huang, H., Tang, H., Wang, J., & Liu, C. (2022). MUSTFN: A spatiotemporal fusion method for multi-scale and multi-sensor remote sensing images based on a convolutional neural network. *International Journal of Applied Earth Observation and Geoinformation*, 115, 103113.
- [23] Larosa, S., Cimini, D., Gallucci, D., Di Paola, F., Nilo, S. T., Ricciardelli, E., ... & Romano, F. (2023). A cloud detection neural network approach for the next generation microwave sounder aboard EPS MetOp-SG A1. *Remote Sensing*, 15(7), 1798.
- [24] Al-Ruzouq, R., Gibril, M. B. A., Shanableh, A., Kais, A., Hamed, O., Al-Mansoori, S., & Khalil, M. A. (2020). Sensors, features, and machine learning for oil spill detection and monitoring: A review. *Remote Sensing*, 12(20), 3338.
- [25] O'carroll, A. G., Armstrong, E. M., Beggs, H. M., Bouali, M., Casey, K. S., Corlett, G. K., ... & Wimmer, W. (2019). Observational needs of sea surface temperature. *Frontiers in Marine Science*, 6, 420.
- [26] Li, W., Hsu, C. Y., & Tedesco, M. (2024). Advancing Arctic sea ice remote sensing with AI and deep learning: now and future. *EGUsphere*, 2024, 1-36.
- [27] Janga, B., Asamani, G. P., Sun, Z., & Cristea, N. (2023). A Review of Practical AI for Remote Sensing in Earth Sciences. *Remote Sensing*, 15(16), 4112.
- [28] Chauhan, S., & Jethoo, A. S. (2023). Thermal characterization of Ajmer city: insights into urban heat dynamics. *Materials Today: Proceedings*.
- [29] Orusa, T., Viani, A., Borgogno-Mondino, E. (2024). Earth Observation Data and Geospatial Deep Learning AI to Assign Contributions to European Municipalities Sen4MUN: An Empirical Application in Aosta Valley (NW Italy). *Land*, 13(1), 80.
- [30] Shao, Z., Cai, J., Fu, P., Hu, L., Liu, T. (2019). Deep learning-based fusion of Landsat-8 and Sentinel-2 images for a harmonized surface reflectance product. *Remote Sensing of Environment*, 235, 111425.
- [31] Kim, S., Lee, S. J., Lee, Y. W. (2020). Retrieval of land surface temperature using Landsat 8 images with deep neural networks. *Korean Journal of Remote Sensing*, 36(3), 487-501.
- [32] Pande, C. B., Egbueri, J. C., Costache, R., Sidek, L. M., Wang, Q., Alshehri, F., ... Pal, S. C. (2024). Predictive modeling of land surface temperature (LST) based on Landsat-8 satellite data and machine learning models for sustainable development. *Journal of Cleaner Production*, 444, 141035.
- [33] Wang, X., Zhong, L., Ma, Y. (2022). Estimation of 30 m land surface temperatures over the entire Tibetan Plateau based on Landsat-7 ETM+ data and machine learning methods. *International Journal of Digital Earth*, 15(1), 1038-1055.
- [34] Vanhellemont, Q. (2020). Combined land surface emissivity and temperature estimation from Landsat 8 OLI and TIRS. *ISPRS Journal of Photogrammetry and Remote Sensing*, 166, 390-402.
- [35] Sekertekin, A., Arslan, N., Bilgili, M. (2020). Modeling diurnal Land Surface Temperature on a local scale of an arid environment using artificial Neural Network (ANN) and time series of Landsat-8 derived spectral indexes. *Journal of Atmospheric and Solar-Terrestrial Physics*, 206, 105328.
- [36] Jia, H., Yang, D., Deng, W., Wei, Q., Jiang, W. (2021). Predicting land surface temperature with geographically weighed regression and deep learning. *Wiley Interdisciplinary Reviews: Data Mining and Knowledge Discovery*, 11(1), e1396.
- [37] Wang, H., Mao, K., Yuan, Z., Shi, J., Cao, M., Qin, Z., ... Tang, B. (2021). A method for land surface temperature retrieval based on model-data-knowledge-driven and deep learning. *Remote sensing of environment*, 265, 112665.
- [38] Ye, X., Liu, R., Hui, J., Zhu, J. (2023). Land Surface Temperature estimation from Landsat-9 thermal infrared data using ensemble learning method considering the physical radiance transfer process. *Land*, 12(7), 1287.